

16

Applications of particle detectors outside particle physics

There are no such things as applied sciences, only applications of science.

Louis Pasteur

There is a large number of applications for radiation detectors. They cover the field from medicine to space experiments, high energy physics and archaeology [1–4].

In medicine and, in particular, in nuclear medicine, imaging devices are usually employed where the size and function of the inner organs can be determined, e.g. by registering γ rays from radioactive tracers introduced into the body.

In geophysics it is possible to search for minerals by means of natural and induced γ radioactivity.

In space experiments one is frequently concerned with measuring solar and galactic particles and γ rays. In particular, the scanning of the radiation belts of the Earth (Van Allen belts) is of great importance for manned space missions. Many open questions of astrophysical interest can only be answered by experiments in space.

In the field of nuclear physics, methods of α -, β - and γ -ray spectroscopy with semiconductor detectors and scintillation counters are dominant [5]. High energy and cosmic-ray physics are the main fields of application of particle detectors [6–11]. On the one hand, one explores elementary particles down to dimensions of 10^{-17} cm, and on the other, one tries by the measurement of PeV γ rays (10^{15} eV) to obtain information on the sources of cosmic rays.

In archaeology absorption measurements of muons allow one to investigate otherwise inaccessible structures, like hollow spaces such as chambers in pyramids. In civil and underground engineering, muon absorption measurements allow one to determine the masses of buildings.

In the following, examples of experiments are presented which make use of the described detectors and measurement principles.

16.1 Radiation camera

The imaging of inner organs or bones of the human body by means of X rays or γ radiation is based on the radiation's specific absorption in various organs. If X rays are used, the image obtained is essentially a shadow recorded by an X-ray film or any other X-ray position-sensitive detector. X rays are perfectly suited for the imaging of bones; the images of organs, however, suffer from a lack of contrast. This is related to the nearly identical absorption characteristics of tissue and organs.

In the early days [12] X rays were just imaged with simple X-ray films. Figure 16.1 shows the first picture ever taken with X rays [13]. In comparison, Fig. 16.2 shows a modern X-ray image of the hands [14]. X-ray imaging is still a very important tool in medical diagnostics. The imaging of bones is a standard technique. However, modern X-ray devices also allow the imaging of tissue; e.g., in mammography very small microcalcifications as early indications of breast cancer can be detected with X rays.



Fig. 16.1. The hand of Mrs Röntgen: the first X-ray image, 1895 [13].



Fig. 16.2. Modern X-ray image of the hands [14].

Even though other techniques of radiation cameras [15], to be described in the following, are powerful tools in medical diagnosis, X-ray imaging is still the choice of the day for many applications.

If organ functions are to be investigated, radioactive tracers can be administered to the patient. These radionuclides, properly integrated into some molecule, will be deposited specifically in certain organs, thereby supplying an image of the organ and its possible malfunctions. Possible tracers for the skeleton are ^{90}Sr , for the thyroid gland ^{131}I or ^{99}Tc , for the kidney again ^{99}Tc and ^{198}Au for the liver. In general, it is advisable to use γ -emitting tracers with short half-lives to keep the radiation load on the patient as low as possible. The γ radiation emitted from the organ under investigation has to be recorded by a special camera so that its image can be reconstructed, e.g. by a scintillation camera introduced by Anger in 1957 [16].

A single small γ -ray detector, e.g. a scintillation counter, has fundamental disadvantages because it can only measure the activity of one picture element (pixel) at a time. In this method, much information remains unused, the time required for a complete picture of the organ is impractically long and the radiation load for the patient is large if many pixels have to be measured – and this is normally necessary for an excellent spatial resolution.

Therefore, a *gamma camera* was developed which allows one to measure the total field of view with a single large-area detector. Such a system, however, also requires the possibility to detect and reconstruct the point of origin of the γ rays. One can use for this purpose a large NaI(Tl) inorganic scintillator, which is viewed by a matrix of photomultipliers

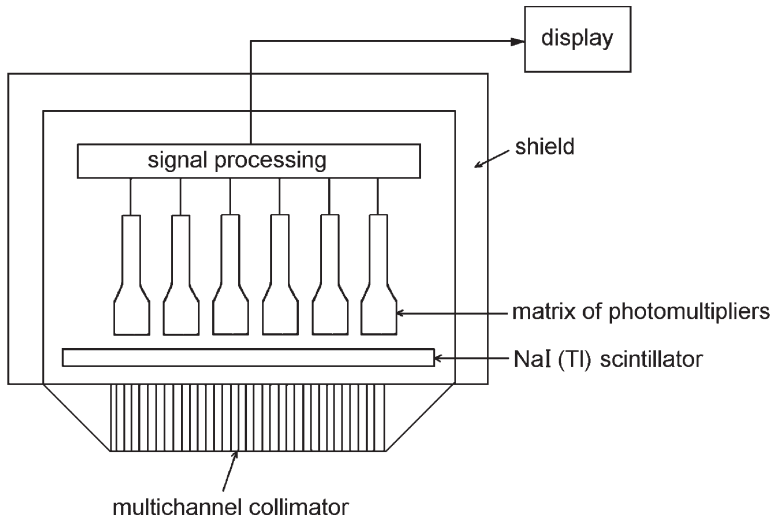


Fig. 16.3. Sketch of a large-area gamma camera [3, 17].

(Fig. 16.3, [3, 17]). Gamma radiation coming from the human body is collimated by a multichannel collimator to maintain the information about the direction of incidence. The amount of light recorded by a certain photomultiplier is linearly related to the γ activity of the organ part positioned beneath it. The light information of the photomultipliers provides a projected image of the organ based on its specific absorption for the γ -radiating tracer. Organ malfunctions are recognised by a characteristic modification of the γ activity.

The dose for the patient can be reduced if every photon can be used for image reconstruction. This is the aim of *Compton cameras* which can provide excellent image qualities at the expense of requiring complicated reconstruction algorithms. Compton cameras or Compton telescopes are also used in γ -ray astronomy [18].

Positron emission tomography (PET) provides a means to reconstruct three-dimensional images of an organ. This method uses positron emitters for imaging. The positrons emitted from the radionuclides will stop within a very short range (\approx mm) and annihilate with an electron from the tissue into two monoenergetic γ rays,



Both γ rays have 511 keV energy each, since the electron and positron masses are completely converted into radiation energy. Because of momentum conservation the γ rays are emitted back to back. If both γ rays are recorded in a segmented scintillation counter, which completely surrounds

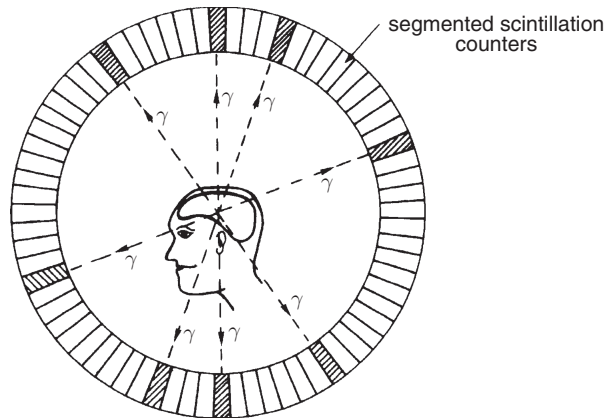


Fig. 16.4. Sketch of a positron emission tomograph. The scintillation counters are also segmented in the longitudinal direction.

the organ to be investigated, the γ rays must have been emitted from a line connecting the two fired modules. By measuring a large number of γ pairs, the three-dimensional structure of the organ can be reconstructed and its possible malfunctions can be recognised (Fig. 16.4).

PET technology is also an excellent tool to probe, e.g. the structure of the brain, far more powerful than is possible by an electroencephalogram (EEG). In a PET scan, where blood or glucose is given a positron emitter tag and injected into the bloodstream of the patient, the brain functions can be thoroughly investigated. If the patient is observed performing various functions such as seeing, listening to music, speaking or thinking, the particular region of the brain primarily responsible for that activity will be preferentially supplied with the tagged blood or glucose to provide the energy needed for the mental process. The annihilation γ rays emitted from these regions of mental activity allow one to reconstruct detailed pictures of regional brain glucose uptake, highlighting the brain areas associated with various mental tasks [19, 20]. The characteristic γ rays of the tagging radioisotope or the 511 keV radiation from positron annihilation can be measured with a high-resolution scintillation counter (NaI(Tl) or BGO) or semiconductor counter (high-purity germanium detector). The mental activity is directly proportional to the local brain radioactivity. Figure 16.5 shows the different response of a human to language and music [21].

This technique does not only allow to image mental processes but it can also be used to identify malfunctions of the brain because the tagged blood or glucose is differently processed by healthy and diseased tissue.

Commonly used positron emitters integrated into radiopharmaceutical compounds include ^{11}C (half-life 20.4 minutes), ^{15}O (2.03 minutes), ^{18}F

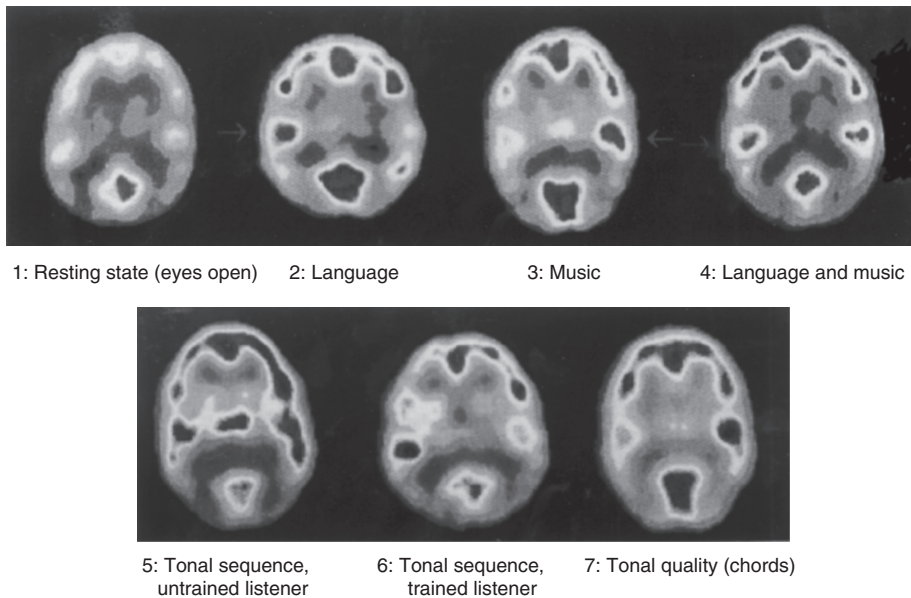


Fig. 16.5. Different response of the human brain to language and music [21].

(110 minutes), ^{75}Br (98 minutes), ^{76}Br (16 hours), ^{86}Y (14.7 hours), ^{111}In (2.8 days), ^{123}Xe (2.08 hours), and ^{124}I (4.15 days). Positron sources typically used in high energy physics for calibration, e.g. ^{22}Na (2.6 years), cannot be used for PET technology, because of their long half-life. To get reasonable images with isotopes like ^{22}Na , high-activity sources would have to be used, which would present an unacceptable high radiation dose for the patient. Therefore, one has to find a compromise between activity, radiation dose, half-life and compatibility with metabolic activity. It is important that the radioisotopes are integrated into molecules that in the ideal case are suitable and selective for the human organ under investigation; e.g., ^{11}C is easily integrated into sugar molecules, and sodium fluoride can also be used as pharmaceutical compound [22].

16.2 Imaging of blood vessels

X-ray images of the chest clearly show the spinal column and the ribs, but the heart or the blood vessels are hardly visible. The reason for missing the blood vessels is that physicswise they are not different from the surrounding tissue, so that there is no image contrast.

An injection of iodine into the blood vessels under investigation enhances the contrast significantly, because of the strong absorption of X rays by iodine ($Z = 53$, absorption cross section $\propto Z^5$). The image

quality can be much improved exposing the patient to X rays with energy just below the K-absorption edge of iodine and to X rays with energy just above the K edge of iodine (Fig. 16.6). The absorption cross section of tissue varies smoothly across the K edge of iodine, while the iodine attenuates X rays just above the K edge much stronger than below.

The two exposures can be subtracted from each other providing an image of the iodine-containing blood vessel alone (*K-edge subtraction technique* or *dual-energy subtraction angiography*). The working principle of the K-edge subtraction technique is demonstrated in Figs. 16.7–16.9 by

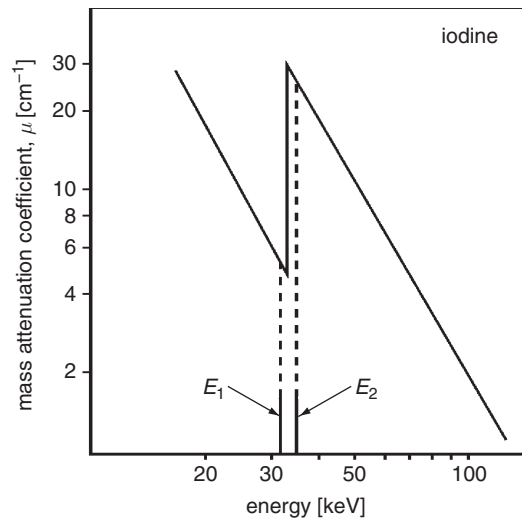


Fig. 16.6. Mass attenuation coefficient by the photoelectric effect in the vicinity of the K edge in iodine.

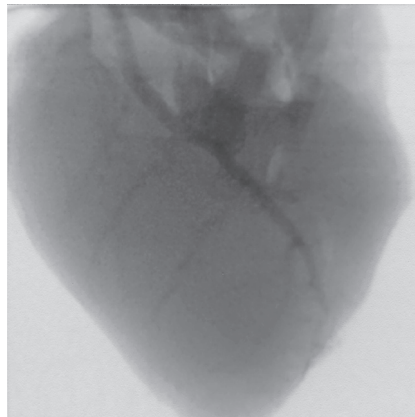


Fig. 16.7. Imaging the structure of a leaf by the K-edge subtraction technique; image taken below the K edge [23, 24].

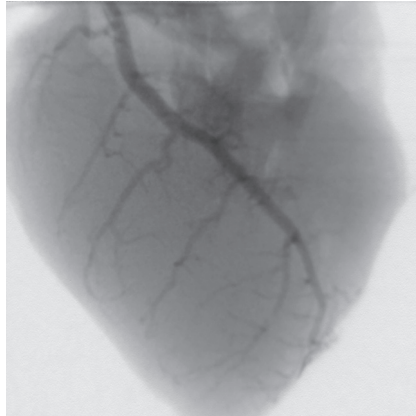


Fig. 16.8. Imaging the structure of a leaf by the K-edge subtraction technique; image taken above the K edge [23, 24].

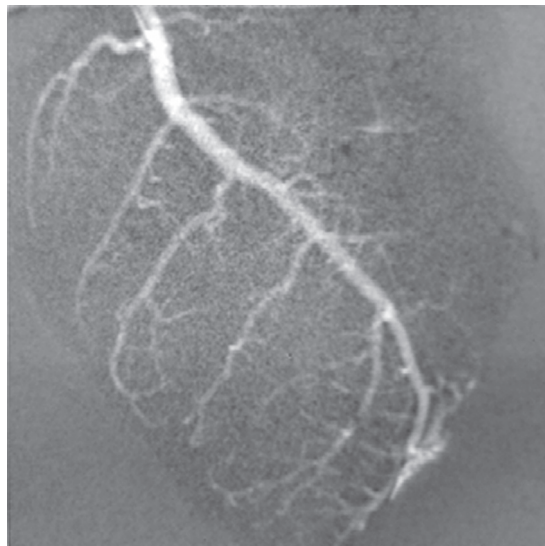


Fig. 16.9. Imaging the structure of a leaf by the K-edge subtraction technique; difference of the images above and below the K edge [23, 24].

imaging the structure of a leaf [23, 24]. Figure 16.10 shows the aorta and coronary arteries in five successive time frames after the iodine injection using this technique [24, 25].

The required two different energies can be selected from a synchrotron-radiation beam by use of two different monochromators. The fans of monochromatised X rays pass through the chest of the patient and are

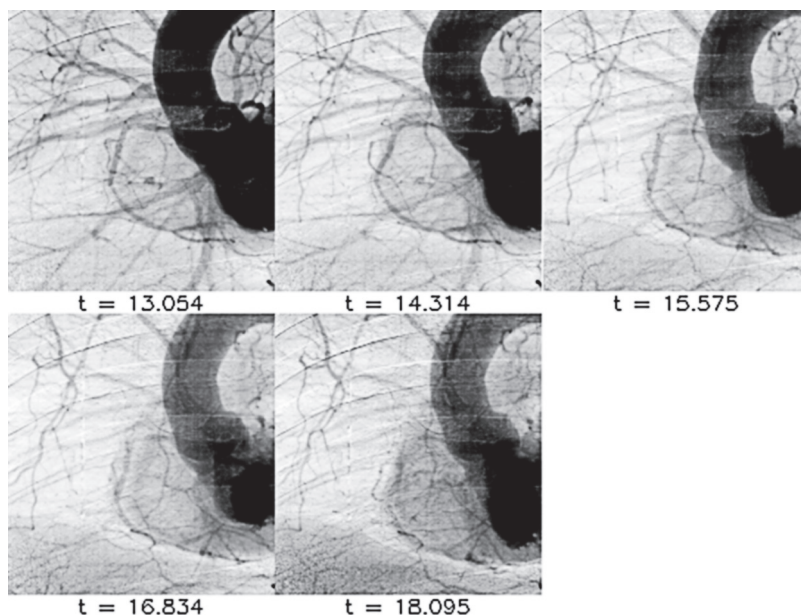


Fig. 16.10. K-edge subtracted images of the human aorta and close-by coronary arteries in five time frames after an iodine injection [24, 25]. The time is given in seconds. The diameter of the human aorta (darkest part) is around 50 mm. The coronary arteries emerge from the aorta with typical diameters of 3 mm to 5 mm narrowing down to 1 mm and below.

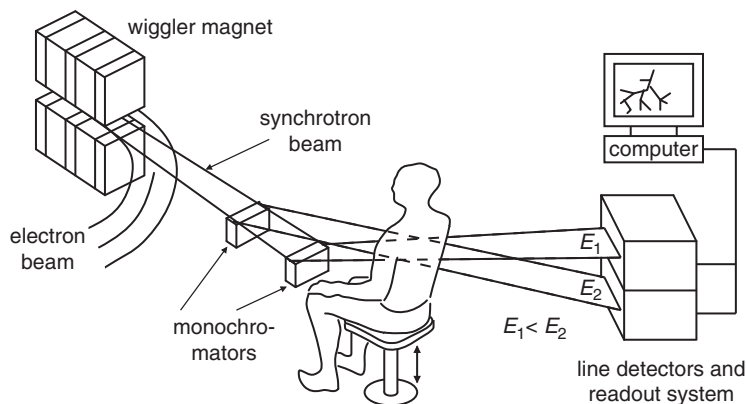


Fig. 16.11. Preparation of two monochromatic synchrotron beams for the imaging of blood vessels [26–28].

detected in an X-ray detector (Fig. 16.11). In clinical applications of this technique multiwire proportional or drift chambers have been used. Even better resolutions can be obtained with micropattern detectors for the detection of the X rays.

16.3 Tumour therapy with particle beams

It has been known for a long time that tissue, in particular tumour tissue, is sensitive to ionising radiation. Therefore, it is only natural that tumours have been treated with various types of radiation like γ rays and electrons. γ rays are easily available from radioactive sources like ^{60}Co and electrons can be accelerated to MeV energies by relatively inexpensive linear accelerators. The disadvantage of γ rays and electrons is that they deposit most of their energy close to the surface. To reduce the surface dose and to optimise the tumour treatment requires rotating the source or the patient so that the surface dose is distributed over a larger volume. In contrast, protons and heavy ions deposit most of their energy close to the end of the range (Bragg peak, see Fig. 16.12). The increase in energy loss at the Bragg peak amounts to a factor of about 5 compared to the surface dose depending somewhat on the particle's energy. Heavy ions offer in addition the possibility to monitor the destructive power of the beam by observing annihilation radiation by standard PET techniques. The annihilation radiation is emitted by β^+ -active nuclear fragments produced by the incident heavy-ion beam itself.

Other techniques of tumour treatment use negative pions which also benefit from the Bragg peak and even additional energy deposits due to star formation. In addition, tumours can also be treated with neutrons. The target for cell-killing is the DNA (deoxyribonucleic acid) in the cell nucleus. The size of the DNA molecule compares favourably well with

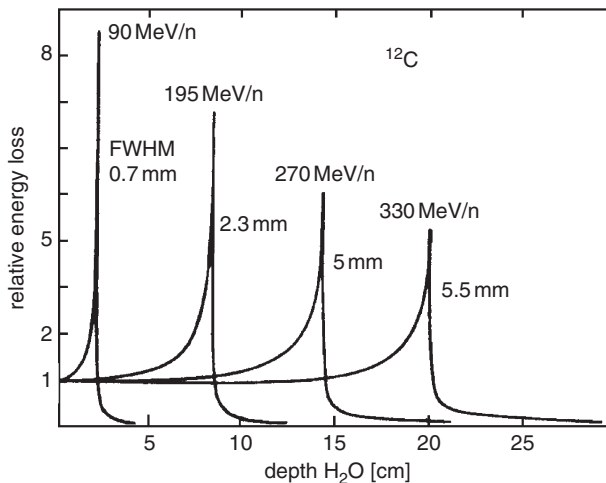


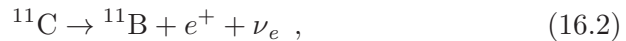
Fig. 16.12. Energy loss of carbon ions ^{12}C in water as a functions of depth [29, 30].

the width of the ionisation track of a heavy ion. The DNA contains two strands containing identical information. A damage of one strand by ionising radiation can easily be repaired by copying the information from the unaffected strand to the damaged one. Therefore, the high ionisation density at the end of a particle's range matches well with the requirement to produce double-strand breaks in the DNA which the cell will not survive.

In *hadron therapy* heavy ions like ^{12}C seem to be optimal for this purpose. Ions heavier than carbon would even be more powerful in destroying tumour tissue, however, their energy loss in the surrounding tissue and in the entrance region already reaches a level where the fraction of irreparable damage is too high, while for lighter ions (like ^{12}C) a mostly reparable damage is produced in the healthy tissue outside the target tumour. The cell-killing rate in the tumour region thus benefits from

- the increased energy loss of protons and ions at the end of the range and
- the increased biological effectiveness due to double-strand breaks at high ionisation density.

The cell-killing rate is eventually related to the equivalent dose H in the tumour region. In addition to the energy loss by ionisation and excitation carbon ions can also fragment leading to the production of lighter carbon ions which are positron emitters. For the ^{12}C case lighter isotopes like ^{11}C and ^{10}C are produced. Both isotopes decay with short half-lives $T_{1/2}(^{11}\text{C}) = 20.38 \text{ min}$, $T_{1/2}(^{10}\text{C}) = 19.3 \text{ s}$ to boron according to



The positrons have a very short range typically below 1 mm. After coming to rest they annihilate with electrons of the tissue giving off two monochromatic photons of 511 keV which are emitted back to back,



These photons can be detected by positron-emission-tomography techniques and can be used to monitor the spatial distribution of the destructive effect of heavy ions on the tumour tissue. These physical and biological principles are employed in an effective way by the *raster-scan technique* [29–32]. A pencil beam of heavy ions (diameter $\approx 1 \text{ mm}$) is aimed at the tumour. The beam location and spread is monitored by tracking chambers with high spatial resolution. In the treatment planning the

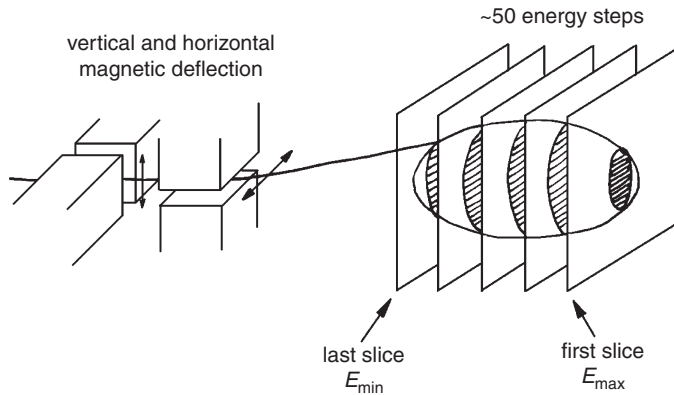


Fig. 16.13. Principle of the raster-scan method [31, 32].

tumour is subdivided into three-dimensional pixels ('voxels'). Then the dose required to destroy the tumour, which is proportional to the beam intensity, is calculated for every voxel. For a fixed depth in tissue an area scan is performed by magnetic deflection sweeping the beam across the area in a similar way as a TV image is produced (Fig. 16.13).

The tumour volume is filled from the back by energy variation (proportional to range variation) of the beam. Typically 50 energy steps are used starting at the rear plane. For a depth profile from 2 cm to 30 cm one has to cover energies from 80 MeV per nucleon to 430 MeV per nucleon. When the beam energy is reduced the required dose for the plane under irradiation is calculated using the damage that the more energetic beam had already produced in its entrance region. This ensures that the lateral (caused by magnetic deflection) and longitudinal scanning (by energy variation) covers the tumour completely. The result of such a scan is shown in Fig. 16.14 in comparison to the effect of ^{60}Co γ rays. The superposition of the individual energy-loss distributions for fixed energies results in a uniform dose distribution over the tumour volume.

As explained, the most effective tumour treatment for deep-seated well-localised tumours takes advantage of heavy ions. On the other hand, protons as charged particles also undergo ionisation energy loss producing a Bragg peak at the end of their range. Protons are easily available at accelerators and they are also frequently used for tumour treatment (*proton therapy*). Figure 16.15 shows the relative dose deposition as a function of depth in water for protons in comparison to γ rays, electrons and neutrons.

In earlier investigations on the possibility of tumour treatment with charged-particle beams, pions, especially negative pions, have also been used for this kind of treatment. Just as protons and heavy ions, pions

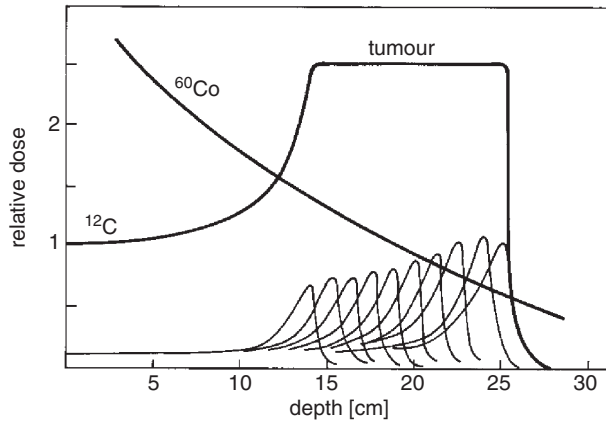


Fig. 16.14. Superposition of individual energy-loss distributions resulting in a uniform dose profile in the tumour region [29].

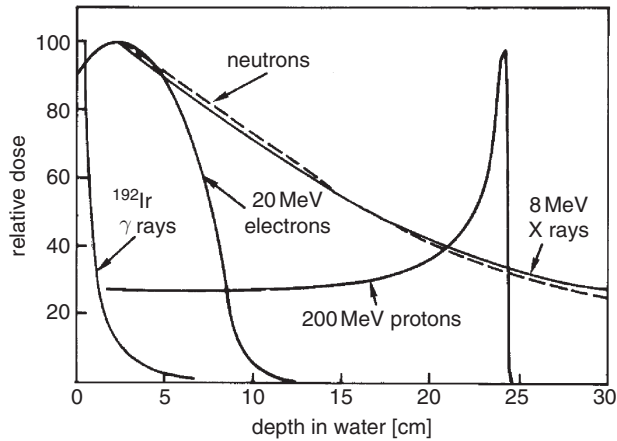


Fig. 16.15. Comparison of depth-dose curves for neutrons, γ rays (produced by a 8 MV-driven X-ray tube), 200 MeV protons, 20 MeV electrons and ^{192}Ir γ rays (161 keV) [33].

lose their energy in matter by ionisation. Up to the end of their range their energy loss is relatively small. At the end of the range their energy loss increases considerably in very much the same way as for protons and heavy ions. In addition, negative pions are captured by atoms forming pionic atoms. By cascade transitions the pions reach orbitals very close to the nucleus and, finally, they are captured by the nucleus. This process is much faster than the decay of free pions. A large number of light fragments like protons, neutrons, Helium-3, Tritons (= ^3H) and α particles can result from pion capture which is called *star formation*. The fragments

will deposit their energy locally at the end of the pions' range. In addition the relative biological effectiveness of the fragments is rather high. Because of this effect, the Bragg peak of ionisation is considerably amplified. The depth profile of the energy deposition of negative pions showing the contributions of various mechanisms can be seen from Fig. 16.16.

The relative biological effectiveness of negative pions was measured in vivo and determined to be about a factor of 3. In addition to the much more favourable depth profile compared to γ rays, one therefore gains about a factor of 3 in destructive power for sick tissue.

In addition to *radiotherapy* with charged particles fast neutrons are used for the treatment of brain tumours. The neutron treatment works along the following lines: the tumour is sensitised with a boron compound before neutron treatment is started. Neutrons have a large cross section for the reaction



In this interaction short-range α particles with a high biological effectiveness are produced. In this neutron-induced reaction α particles of 2 MeV with a range of several microns are generated. This ensures that the

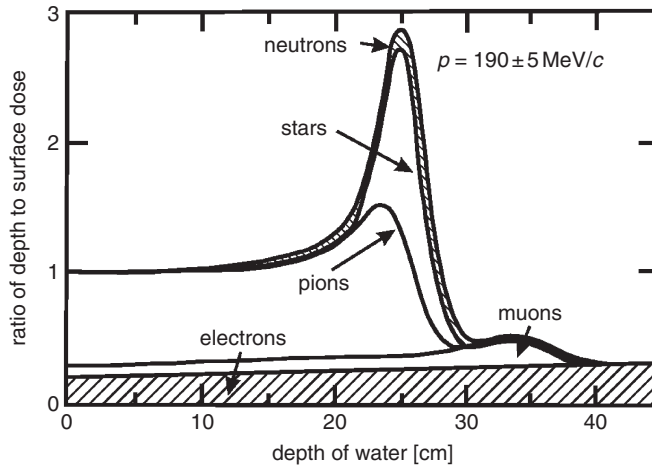


Fig. 16.16. Depth profiles of the energy deposition of a beam of negative pions with a small admixture of muons and electrons. The particle momentum is $190 \pm 5 \text{ MeV}/c$. The pion ionisation-loss contribution is marked as 'pions', while 'stars' and 'neutrons' indicate the contributions from nuclear fragments and neutrons produced in pion nuclear interactions, respectively. The small contribution of muons and electrons originates from the contamination of muons and electrons in the negative pion beam [3, 34]. The relative biological effectiveness of muons and electrons was assumed to be unity.

destructive action of the α particles is limited to the local tissue. Clinical tests have shown that best results are obtained with epithermal neutrons (approximately 1 keV). Such neutron beams can be produced by interaction of 5 MeV protons on light target materials, e.g. lithium or beryllium.

A possible direct irradiation with neutrons without sensitising the tumour has the clear disadvantage that neutrons show a similar dose-depth curve like ^{60}Co γ rays thus producing a high amount of biologically very effective damage in the healthy tissue around the tumour.

The ionisation-dose profile of charged particles has been known for a long time from nuclear and particle physics. The instrumentation originally developed for elementary particle physics experiments has made it possible to design and monitor particle beams with great precision which can then be used for tumour therapy. Heavy ions seem to be ideal projectiles for tumour treatment. They are suitable for well-localised tumours. The availability of *treatment facilities* is increasing [31]. Naturally, such a facility requires an expensive and complex accelerator for charged particles. For beam steering and control sophisticated particle detectors and interlock systems are necessary to ensure the safety of patients.

16.4 Surface investigations with slow protons

A large number of non-destructive methods exist to determine the chemical composition of surfaces, one possibility being *proton-induced X-ray emission* (PIXE). If slow charged particles traverse matter, the probability for nuclear interactions is rather low. In most cases the protons lose their kinetic energy by ionising collisions with atoms. In these ionisation processes electrons from the K, L and M shells are liberated. If these shells are filled by electron transitions from higher shells, the excitation energy of the atom can be emitted in form of characteristic X rays. This X-ray fluorescence represents a fingerprint of the target atom. Alternatively, the excitation energy of the atomic shell can be directly transferred radiationless to an electron in one of the outer shells which then can escape from the atom as Auger electron. With increasing atomic number the emission probability ('yield') of characteristic X rays increases with respect to the Auger-electron emission probability. It varies between 15% at $Z = 20$ and reaches nearly 100% for $Z \leq 80$. On the other hand – if the Auger electrons and their energy are measured – their kinetic energy is also a characteristic of the atom and can be used for identification. This Auger-electron spectroscopy (AES) [35] works, however, only for very thin samples because the range of the low-energy electrons is rather short.

The overall photon yield per incident proton depends on the properties of the target, like atomic number, density and thickness of the sample.

The total photon yield can be controlled by the intensity of the primary proton beam.

The measurement of proton-induced characteristic X rays is – quite in contrast to the application of electrons – characterised by a low background of bremsstrahlung. The probability for proton bremsstrahlung is negligible. Only a very low-intensity continuous spectrum will be produced by bremsstrahlung of δ electrons created by the protons. Therefore, the characteristic X rays can be studied in a simple, clear and nearly background-free environment.

The X rays can be recorded in lithium-drifted silicon semiconductor counters, which are characterised by a high energy resolution. An experimental set-up of a typical PIXE system is sketched in Fig. 16.17 [36].

A proton beam of several μA with typical energies of several MeV traverses a thin aluminium scattering foil, which widens the proton beam without a sizeable energy loss. The beam is then collimated and impinges on a selected area of the material to be investigated. A step motor provides a means to move the sample in a well-defined way. This is required to investigate the homogeneity of an alloy over large areas.

The energy of characteristic X rays increases with the atomic number Z according to

$$E_K \propto (Z - 1)^2 \quad (16.6)$$

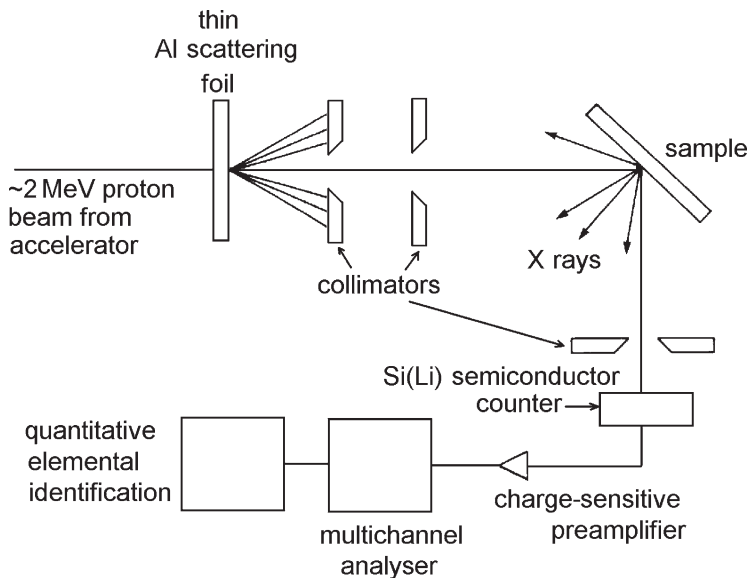


Fig. 16.17. Set-up of a PIXE detector for the investigation of surface structure with slow protons [36].

(*Moseley's law*). The energy resolution of a scintillation counter and certainly that of a silicon lithium-drifted semiconductor counter is sufficient to separate characteristic X rays of elements with Z differing by only 1 unit. Elements from phosphorus ($Z = 15$) up to lead ($Z = 82$) can be identified by this method down to concentrations of less than 1 ppm ($= 10^{-6}$).

The PIXE technique is increasingly applied in the fields of biology, materials science, art and archaeology, and in all cases where a quick, sensitive, non-destructive method of surface investigation is required.

16.5 Gamma- and neutron-backscatter measurements

Measurements to determine the level of some material in a container are based on absorption techniques. Normally, they are performed under well-defined conditions in a laboratory. In applications in geology, for example, in the investigation of boreholes, mainly the chemical composition of the material in the walls of the borehole is of interest. This is particularly true in the search for deposits of certain materials, e.g. oil or rare metals.

Such a search can be done by the *gamma-backscatter method* (Fig. 16.18): a radioactive source like ^{226}Ra emits 186 keV γ rays

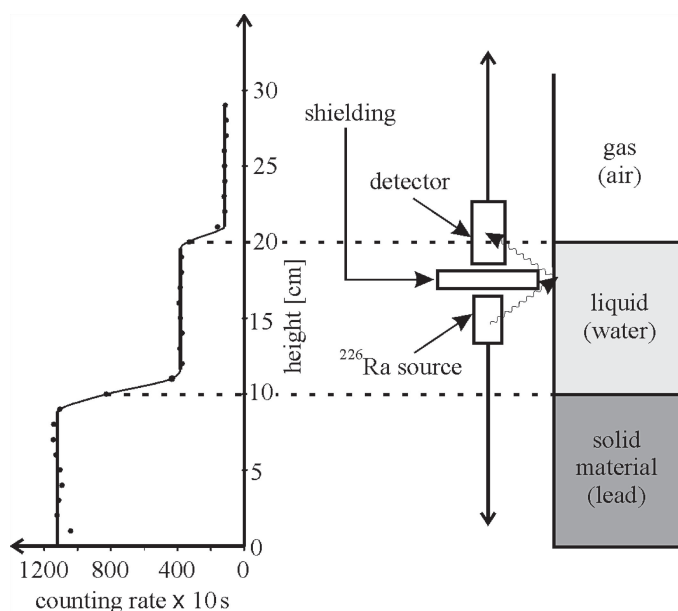


Fig. 16.18. Gamma-backscatter method for the identification of physicochemical properties of deposits [37].

isotropically. A scintillation counter records γ rays backscattered from the surrounding material. The detector itself is shielded against direct radiation from the source. The cross section for backscattering depends on the density and atomic number of the borehole material. Figure 16.18 demonstrates the working principle of this technique [37]. The counting rate of the scintillation counter as a function of the height reflects the different materials in the layer consisting of lead, water and air. The profile of the backscatter intensities exhibits clear element-specific differences. The experimentally determined backscatter rates therefore allow to infer informations on the density and chemical abundance of the scattering material. Sample measurements on air, water, aluminium, iron and lead show a clear correlation between the backscatter intensity and the product of density ρ and atomic number Z . The backscatter intensities can be fitted over a wide range by the function $R \propto (\rho \cdot Z)^{0.2}$ (Fig. 16.19 [37]).

In very much the same way borehole investigations can be done using the *neutron-backscatter technique* [38, 39]. Fast neutrons emitted from an artificial neutron source are scattered in the surrounding material. The scattering cross section associated with high energy transfer is largest for low atomic numbers. Since oil contains hydrogen in form of hydrocarbons, oil is very effective in slowing down the neutrons. If oil is present, the flux of slow neutrons will be high close to the source while in the absence of oil the fast neutrons will hardly be moderated. The intensity ratio of two measurements – one near the source, the other at some distance (60–80 cm) – provides information on the hydrogen concentration near the borehole. The measurement of the backscattered neutrons can be done with BF_3 counters or scintillation counters made from LiI.

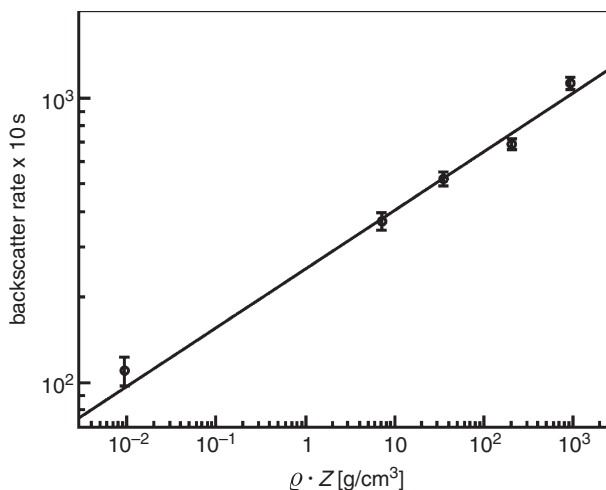


Fig. 16.19. Material dependence of the gamma-backscatter rate [37].

In addition to the neutron-backscatter measurement, gamma rays emitted from nuclei after neutron capture can also be used as an indicator for the chemical configuration of the borehole material. For a clear identification of the scattering material the energies of the gamma rays have to be accurately measured, since these energies are characteristic for the scattering nuclei and can serve as fingerprints for the chemical abundance in the borehole.

Also *aerial surveys* are possible to locate, e.g. uranium deposits [39]. Radiation detectors can be carried on board of planes or helicopters to scan large areas in relatively short periods. As detectors, large-area scintillation counters ($10 \times 10 \times 40 \text{ cm}^3$, NaI(Tl), CsI(Tl), BGO) can be used. The detection of 1.46 MeV γ rays from ^{40}K decays or daughters from the uranium or thorium decay series indicate the presence of uranium. The existence of ^{40}K along with uranium and thorium in natural ores is often the result of the same geochemical conditions that concentrated the main mineral-bearing ores. The identification of these characteristic γ -ray emitters only requires scintillation detectors with moderate resolution. This is because the low-energy γ rays from ^{230}Th (67.7 keV) and ^{238}U (49.6 keV) are well separated from the ^{40}K emission line (1461 keV).

16.6 Tribology

Tribology deals with the design, friction, wear and lubrication of interacting surfaces in relative motion as, e.g., in bearings or gears. For the investigation of such processes radioactive tracers present distinctive advantages. One of the strong points of using radioactive elements for tribology is the extreme sensitivity. Quantities as low as 10^{-10} g can be detected which can hardly be measured with chemical reactions. Also the wear of surfaces of identical materials (e.g. friction losses of iron on iron) where chemical methods fail completely does not present a problem with radioactive tracer elements.

The idea of *radio-tribology* is that one part involved in the wear or friction process contains a radioactive tag. This can be achieved by coating one component participating in the friction process with a radioactive surface layer. Counting the worn material with a monitor system consisting of a scintillation detector or proportional counter allows to determine the amount of wear. The tagging can also be accomplished by neutron activation of one material involved in the friction investigation. The measurement of the transferred activated material can be also determined by autoradiographic techniques. This would also allow to identify the positions where maximum wear occurs.

In car industries the dependence of the wear on special lubricants is of particular interest. Valve-seat-wear measurements show a distinct dependence on the oil used for lubrication. Figure 16.20 shows the valve moving through a seat that contains an activated zone. The amount of wear can be determined from the activity in the lubricant.

The measurement of the time-dependent wear of the valve seat allows to get information about the long-term behaviour of the oil. The on-line-recorded activity also permits to derive a warning for the due oil exchange.

Similar techniques can also be used for all kinds of gear and bearings. As an example, Fig. 16.21 shows the influence of the motor oil on crankshaft wear. The oil labelled 5 is obviously the best. However, the lubrication deteriorates after 100 h of operation.

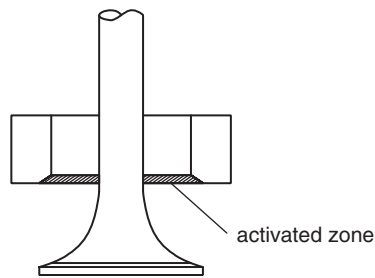


Fig. 16.20. Schematic drawing showing the valve moving through a partially activated zone of the valve seat [40].

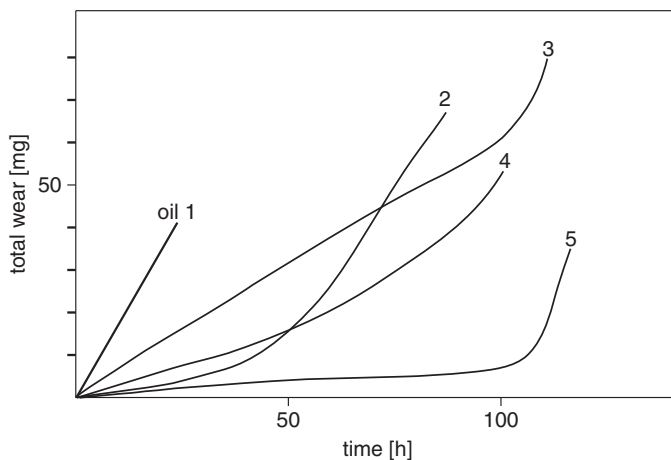


Fig. 16.21. Influence of different motor-oil products on crankshaft wear [40, 41].

16.7 Identification of isotopes in radioactive fallout

The γ -ray spectrum of a mixture of isotopes can be used to determine quantitatively the radionuclides it contains. Detectors well suited for this application are high-resolution germanium semiconductor counters, into which lithium ions have been drifted, or high-purity germanium crystals. The atomic number of germanium is sufficiently large so that the γ rays emitted from the sample are absorbed with high probability via photoelectric effect, thereby producing distinct γ -ray lines. The well-defined photopeaks or full-absorption peaks are used for the identification of the radioisotope. Figure 16.22 shows part of the γ -ray spectrum of an air filter shortly after the reactor accident in Chernobyl [42]. Apart from the γ -ray lines originating from the natural radioactivity, some *Chernobyl isotopes* like ^{137}Cs , ^{134}Cs , ^{131}I , ^{132}Te and ^{103}Ru are clearly recognisable by their characteristic γ energies.

The identification of pure β -ray emitters, which cannot be covered with this method, is possible with the use of silicon lithium-drifted semiconductor counters. Because of their relatively low atomic number ($Z = 14$), these detectors are relatively insensitive to γ rays. β -ray emitting isotopes can be quantitatively determined by a successive subtraction of calibration spectra. The identification of the isotopes is based on the characteristic maximum energies of the continuous β -ray spectra. The maximum energies can best be determined from the linearised electron spectra (Fermi–Kurie plot) [43].

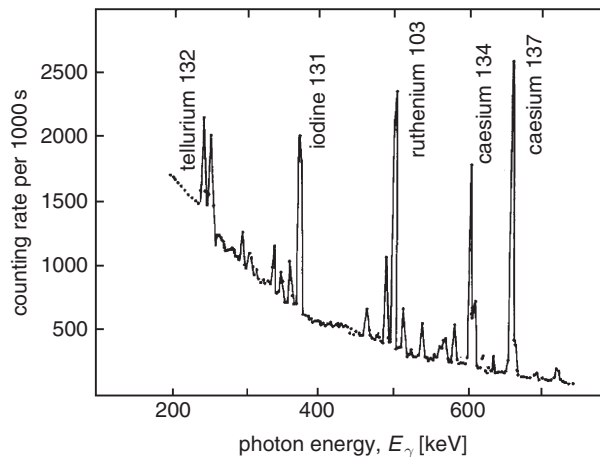


Fig. 16.22. Part of the γ spectrum of a radioactive air filter (the γ energies of some ‘Chernobyl isotopes’ are indicated) [42].

16.8 Search for hidden chambers in pyramids

In the large Cheops pyramid in Egypt several chambers were found: the King's, Queen's, underground chamber and the so-called 'Grand Gallery' (Fig. 16.23). In the neighbouring Chephren pyramid, however, only one chamber, the Belzoni chamber (Fig. 16.24) could be discovered. Archaeologists suspected that there might exist further, undetected chambers in the Chephren pyramid.

It was suggested to 'X ray' the pyramids using muons from cosmic radiation [44]. Cosmic-ray muons can easily penetrate the material of the pyramid. Of course, in this process their intensity is slightly reduced. The intensity reduction is related to the amount of material between the outer wall of the pyramid and the position of the detector. An enhanced

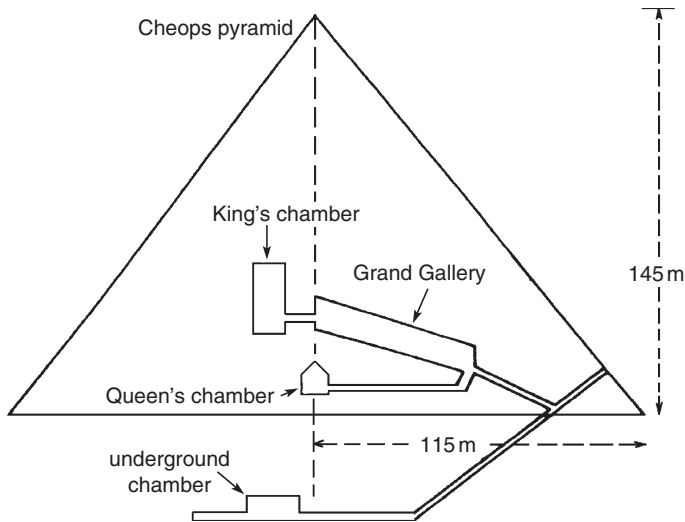


Fig. 16.23. Inner structure of the Cheops pyramid [44], © 1970 by the AAAS.

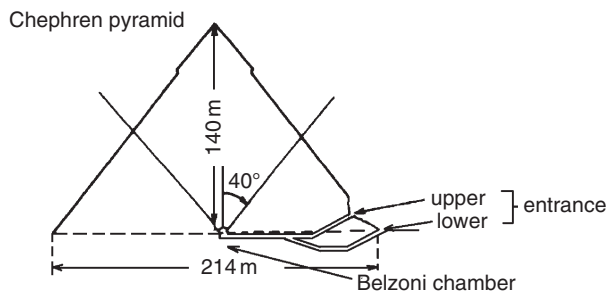


Fig. 16.24. Structure of the Chephren pyramid [44], © 1970 by the AAAS.

relative intensity in a certain direction would indicate the presence of some hollow space which might represent an undiscovered chamber (*muon X-ray technique*).

The intensity of muons as a function of depth $I(h)$ can be approximated by

$$I(h) = k \cdot h^{-\alpha} \quad \text{with } \alpha \approx 2 . \tag{16.7}$$

Differentiating Eq. (16.7) yields

$$\frac{\Delta I}{I} = -\alpha \frac{\Delta h}{h} . \tag{16.8}$$

In the case of the Chephren pyramid muons traversed typically about 100 m material before reaching the Belzoni chamber. Consequently, for an anticipated chamber height of $\Delta h = 5$ m, a relative intensity enhancement compared to neighbouring directions of

$$\frac{\Delta I}{I} = -2 \frac{(-5 \text{ m})}{100 \text{ m}} = 10\% \tag{16.9}$$

would be expected for a muon detector installed in the Belzoni chamber.

The detector used for this type of measurement (Fig. 16.25) consisted of a telescope ($2 \times 2 \text{ m}^2$) of three large-area scintillation counters and four wire spark chambers [44, 45].

The spark-chamber telescope was triggered by a three-fold coincidence of scintillation counters. The iron absorber prevented low-energy muons from triggering the detector. Because of their large multiple-scattering

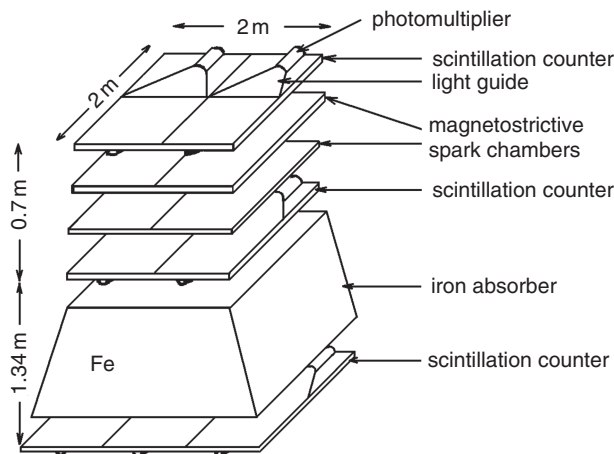


Fig. 16.25. Set-up of a muon-absorption detector for the search for hidden chambers in the Chephren pyramid [44], © 1970 by the AAAS.

angles, low-energy muons would only produce a fuzzy image of possible chambers. Spark chambers with magnetostrictive readout were used for the track reconstruction of the recorded muons.

The detector was installed approximately at the centre of the base of the Chephren pyramid inside the Belzoni chamber (see Fig. 16.24). It had been suspected that just above the Belzoni chamber there might be additional cavities. Therefore, the range of acceptance of the muon telescope was restricted to zenith angles of about 40° with complete azimuthal coverage. The measured azimuthal variation of the intensity for a fixed zenith angle clearly shows the corners of the pyramid, thus proving the working principle of the method. The section of the pyramid scanned by the detector was subdivided into cells of $3^\circ \times 3^\circ$. In total, several million muons were recorded. The azimuthal- and zenith-angle variation of the muon flux was compared to a simulated intensity distribution, which took into account the known details of the pyramid structure and the properties of the detector. This allowed one to determine deviations from the expected muon rates. Since the angular distributions of cosmic-ray muons agreed with the simulation within the statistics of measurement, no further chambers in the pyramid could be revealed. The first measurement only covered a fraction of the pyramid volume, but later the total volume was subjected to a *muon X-ray photography*. This measurement also showed that within the resolution of the telescope no further chambers existed in the Chephren pyramid.

A similar muon X-ray technique has also been used to probe the internal structure and composition of a volcano [46].

16.9 Random-number generators using radioactive decays

The need for random numbers satisfying the highest statistical requirements is increasing. Since the advent of publicly available cryptographic software like *Pretty Good Privacy (PGP)*, there has been discussion about how cryptographic keys should be generated. While PGP uses the time between two keystrokes on a keyboard and the value of the key pressed as a source of randomness, this is clearly not enough when it comes to high-security applications. International laws and decrees governing digital signature schemes require that the keys are truly random. Sources of randomness known to physicists are, e.g. radioactive decays or the noise of a diode. The use of radioactivity is superior over thermal noise, since it is virtually independent of the conditions of the environment (pressure, temperature, chemical environment). To the opposite, thermal noise of diodes is temperature-dependent and the consecutive bits are correlated, so a cryptographic treatment of the random numbers is

needed in order to obtain useful cryptographic keys. If an adversary can gain access to the device using a diode as the source of randomness, he can alter the temperature and therefore change the output. Radioactive decays are much harder to influence and thus more secure to manipulation.

At the heart of such a device a proportional counter can be used. An incandescent mantle containing thorium-232 can serve as radioactive source. Thorium-232 undergoes α decays with 4.083 MeV energy. The rationale behind the use of the incandescent mantle is that the exemption limit for natural radioactive sources like Th-232 is relatively generous. Therefore, such a low-activity source of natural radioactivity does not require special measures and precautions from the point of view of radiation protection. Of course, also other natural radioactive sources like potassium-40 could be used with the same advantage.

Even though the thin walls of the cathode cylinder of the proportional counter absorb most of the α particles, photons from the γ transitions of thorium-232 or its decay products are recorded. The detection of an ionising particle results in a sudden small decline in the applied high voltage. This pulse is fed through a capacitor to an amplifier and from there to a discriminator, which may, or may not, lift the signal to standard TTL level for a certain time (typically 100 ns). Whenever such a low-high transition occurs, a *toggle flip-flop* is read out. A toggle flip-flop periodically changes its state from logical '0' to logical '1' and vice versa and is typically clocked at high frequencies (e.g. 15 MHz). Since the time difference between two pulses from the proportional counter is not predictable, the sequence of output bits from the toggle flip-flop should be random.

The working principle of such a device is shown in Fig. 16.26. Individual signals from the detector whose appearance we believe to be unpredictable in time are shaped and compared in time with the current state of a freely running flip-flop. If the flip-flop is in a logical '1' state when the random signal arrives, the resulting random bit is set to '1'. If the random signal arrives when the flip-flop is in the low state, the random bit is set to '0'. The resulting bits are stored in a buffer and can be accessed and processed by the CPU. The number of outgoing random bits per time unit by this type of device is therefore directly given by the activity of the random source. If the random sequence is used as a cryptographic key material or as a seed for another pseudo-random-number generator, only a low number of random bits per time unit is required and the activity of the chosen radioactive source can be moderate (e.g. a few hundred Bq) [47].

Random numbers can be created in a fast way by using strong sources. It is, however, not necessary that the rates are comparable to the clock

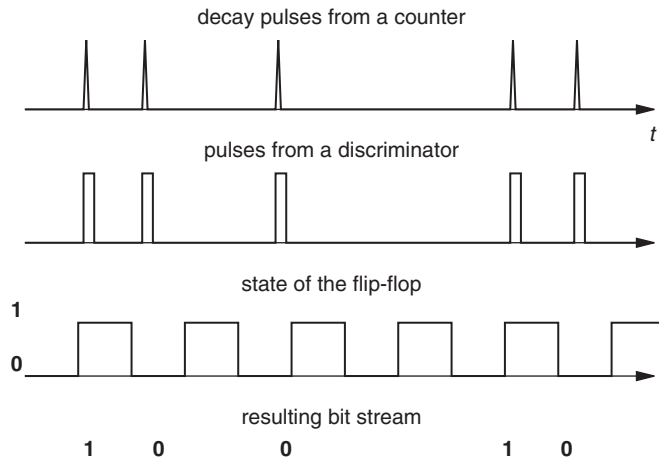


Fig. 16.26. Working principle of the true random-number generator.

frequency. The principle also works with lower intensities at the expense of longer exposure times to create the desired randomness.

The circuitry with the toggle flip-flop can also be shown to be able to produce random bits in a computer simulation. One can use Poisson-distributed pseudo random numbers to simulate the time difference between two radioactive decays. Also the dead time of the counter and the electronics can be integrated into the simulation. Several statistical and cryptographic tests on the simulated data demonstrate that the output bits can be considered random [48, 49].

To investigate how well the simulation agrees with theory, one can, e.g., compare the results for 4-bit patterns with expectation. If one divides a bit string of length n into substrings of length 4, then the 16-bit patterns 0000, 0001, 0010, 0011, \dots , 1111 should occur equally likely.

In very much the same way the particles from a radioactive source can also be replaced by muons from cosmic rays passing through the proportional tube or through a scintillation counter. Consider a bit string generated in this way which consists of substrings of identical bits, either 0s or 1s. Such a substring is called a *run*. A run of 0s is called a *gap*, while a run of 1s is called a *block*. Since the probability for the occurrence of a 0 or 1 in a truly random bit string should be exactly 0.5 and should not depend on the value of the predecessor, one expects to have runs of length 1 with probability $1/2$, runs of length 2 with probability $1/4$, runs of length 3 with probability $1/8$ and so on. In general a run of length k occurs with probability $p_k = 1/2^k$.

The results from different cosmic-ray samples recorded by a plastic scintillator show exactly this behaviour. The exposure times for the different cosmic data sets were on the order of a few seconds. The longer

samples show perfect agreement with expectation for true random numbers, while a short run of only 30 ms does not reproduce the tail of the distribution (blocks or gaps for $k \geq 6$), clearly showing that a certain number of cosmic-ray events is necessary to achieve true randomness. The purpose of the short run was just to show this obvious requirement [48, 49].

A miniaturised device working along this principle (e.g. a 1 cm² small silicon chip) acting as particle detector for γ rays from a naturally occurring radioisotope could easily be integrated into a personal computer providing a *true random-number generator*.

16.10 Experimental proof of $\nu_e \neq \nu_\mu$

Neutrinos are produced in weak interactions, e.g. in the β decay of the free neutron,

$$n \rightarrow p + e^- + \bar{\nu} \quad , \quad (16.10)$$

and in the decay of charged pions,

$$\begin{aligned} \pi^+ &\rightarrow \mu^+ + \nu \quad , \\ \pi^- &\rightarrow \mu^- + \bar{\nu} \quad . \end{aligned} \quad (16.11)$$

(For reasons of lepton-number conservation one has to distinguish between neutrinos (ν) and antineutrinos ($\bar{\nu}$.) The question now arises whether the antineutrinos produced in the β decay and π^- decay are identical particles or whether there is a difference between the electron- and muon-like neutrinos.

A pioneering experiment at the AGS accelerator (Alternating Gradient Synchrotron) in Brookhaven with optical spark chambers showed that electron and muon neutrinos are in fact distinct particles (*two-neutrino experiment*). The Brookhaven experiment used neutrinos from the decay of pions. The 15 GeV proton beam of the accelerator collided with a beryllium target, producing – among other particles – positive and negative pions (Fig. 16.27, [50]).

Charged pions decay with a lifetime of $\tau_0 = 26$ ns ($c\tau_0 = 7.8$ m) into muons and neutrinos. In a decay channel of ≈ 20 m length practically all pions have decayed. The muons produced in this decay were stopped in an iron absorber so that only neutrinos could emerge from the iron block.

Let us assume for the moment that there is no difference between electron and muon neutrinos. Under this assumption, neutrinos would be expected to be able to initiate the following reactions:

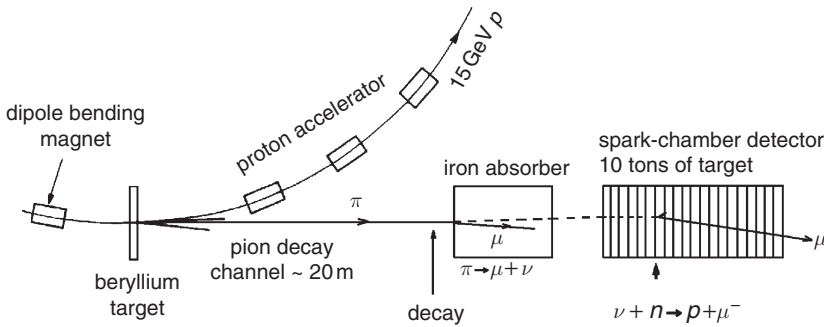


Fig. 16.27. Production of a neutrino beam at the 15 GeV AGS proton synchrotron [50].

$$\begin{aligned}
 \nu + n &\rightarrow p + e^- , \\
 \bar{\nu} + p &\rightarrow n + e^+ , \\
 \nu + n &\rightarrow p + \mu^- , \\
 \bar{\nu} + p &\rightarrow n + \mu^+ .
 \end{aligned}
 \tag{16.12}$$

If, however, electron and muon neutrinos were distinct particles, neutrinos from the pion decay would only produce muons.

The cross sections for neutrino–nucleon interactions in the GeV range are only on the order of magnitude 10^{-38} cm^2 . Therefore, to cause the neutrinos to interact at all in the spark-chamber detector, it had to be quite large and very massive. Ten one-ton modules of optical spark chambers with aluminium absorbers were used for the detection of the neutrinos. To reduce the background of cosmic rays, anti-coincidence counters were installed. The spark-chamber detector can clearly identify muons and electrons. Muons are characterised by a straight track almost without interaction in the detector, while electrons initiate electromagnetic cascades with multiparticle production. The experiment showed that neutrinos from the pion decay only produced muons, thereby proving that electron and muon neutrinos are distinct elementary particles.

Figure 16.28 shows the ‘historical’ record of a neutrino interaction in the spark-chamber detector [50]. A long-range muon produced in the neutrino interaction is clearly visible. At the primary vertex a small amount of hadronic activity is seen, which means that the interaction of the neutrino was inelastic, possibly

$$\nu_\mu + n \rightarrow \mu^- + p + \pi^0 ,
 \tag{16.13}$$

with subsequent local shower development by the π^0 decay into two photons.

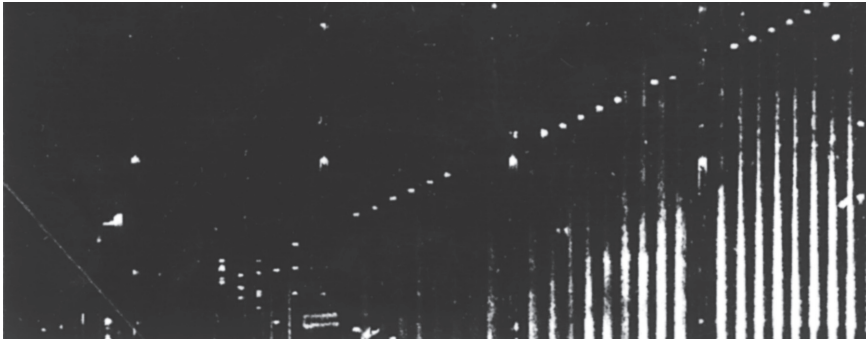


Fig. 16.28. Muon production in a neutrino–nucleon interaction [50, 51].

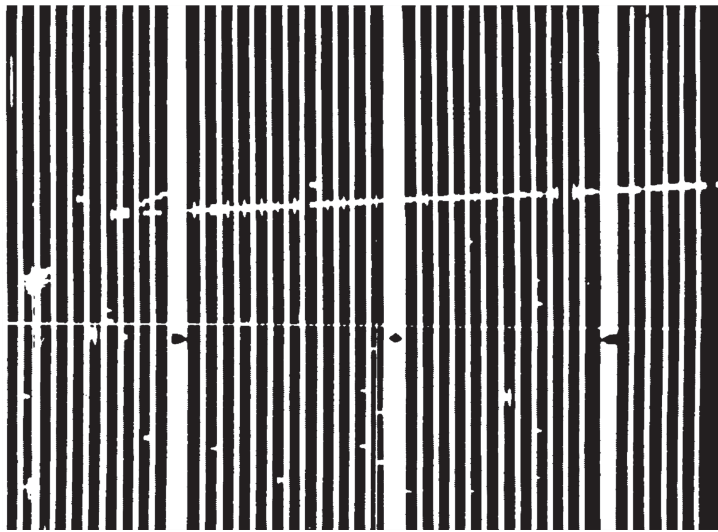


Fig. 16.29. Muon production by muon neutrinos in a multiplate spark chamber in a CERN experiment [52, 53].

Later, the experimental result was confirmed in an experiment at the European Organisation for Nuclear Research (CERN). Figure 16.29 shows a neutrino interaction (ν_μ) in the CERN experiment, in which a high-energy muon is generated via the reaction

$$\nu_\mu + n \rightarrow p + \mu^- , \quad (16.14)$$

which produces a straight track in the spark-chamber system. The recoil proton can also be clearly identified from its short straight track [52, 53].

16.11 Detector telescope for γ -ray astronomy

In the field of γ -ray astronomy the detection of point sources that emit photons in the MeV range and at even higher energies is an interesting topic. The determination of the γ -ray spectra emitted from the source may also provide a clue about the acceleration mechanism for charged particles and the production of energetic γ rays [54, 55]. For energies in excess of several MeV the electron–positron pair production is the dominating photon interaction process. The schematic set-up of a detector for γ -ray astronomy is shown in Fig. 16.30.

The telescope is triggered by a coincidence of elements from the segmented shower counter with an anti-coincidence requirement of the outer veto counter. This selects photons that converted in the tracking device. In the track detector (drift-chamber stack or silicon pixel detector) the produced e^+e^- pair is registered, and the incident direction of the γ ray is reconstructed from the tracks of the electron and positron. The total-absorption scintillator calorimeter can be made from a thick caesium-iodide crystal doped with thallium. Its task is to determine the energy of the γ ray by summing up the energies of the electron–positron pair.

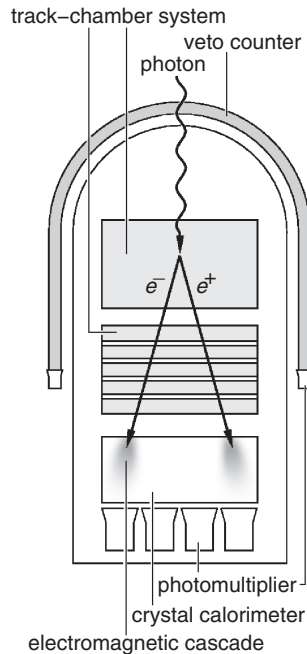


Fig. 16.30. Schematic set-up of a satellite experiment for the measurement of γ rays in the GeV range [56].

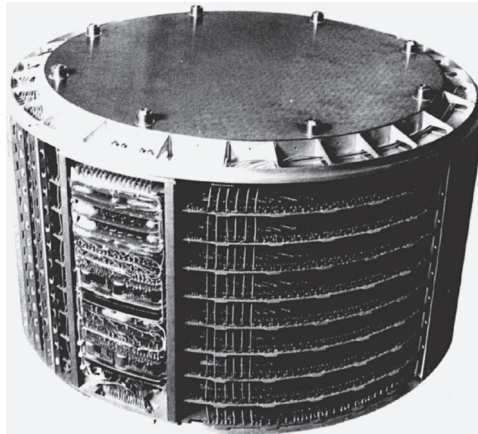


Fig. 16.31. Photograph of the COS-B detector [58].

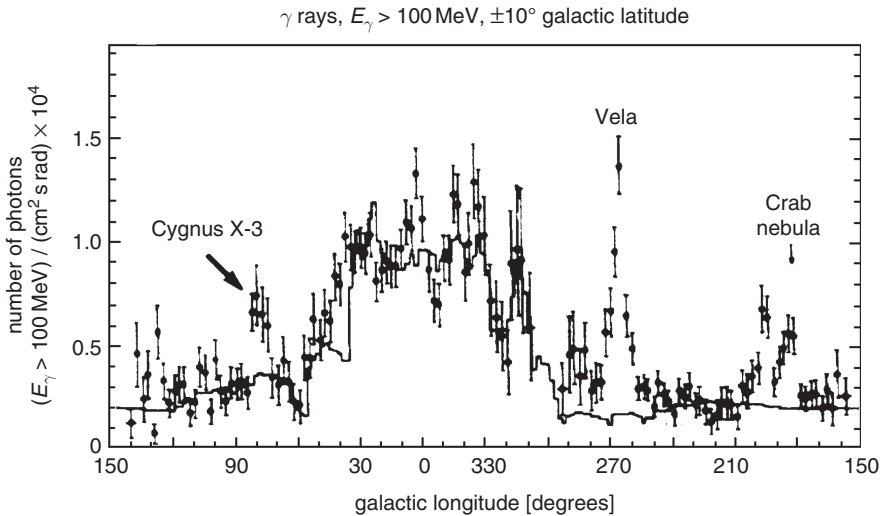


Fig. 16.32. Distribution of γ rays with energies greater than 100 MeV as a function of galactic longitude [59].

In the early days of γ -ray astronomy a spark-chamber telescope (Fig. 16.31) as track detector was used on board the COS-B satellite [57] launched in 1975. It has recorded γ rays in the energy range between $30 \text{ MeV} \leq E_\gamma \leq 1000 \text{ MeV}$ from the Milky Way. COS-B had a highly eccentric orbit with an apogee of 95 000 km. At this distance the background originating from the Earth's atmosphere is negligible.

The COS-B satellite could identify the galactic centre as a strong γ -ray source. In addition, point sources like Cygnus X3, Vela X1, Geminga and the Crab Nebula could be detected [57].

Figure 16.32 shows the intensity distribution of γ rays with energies greater than 100 MeV as a function of the galactic longitude in a band of

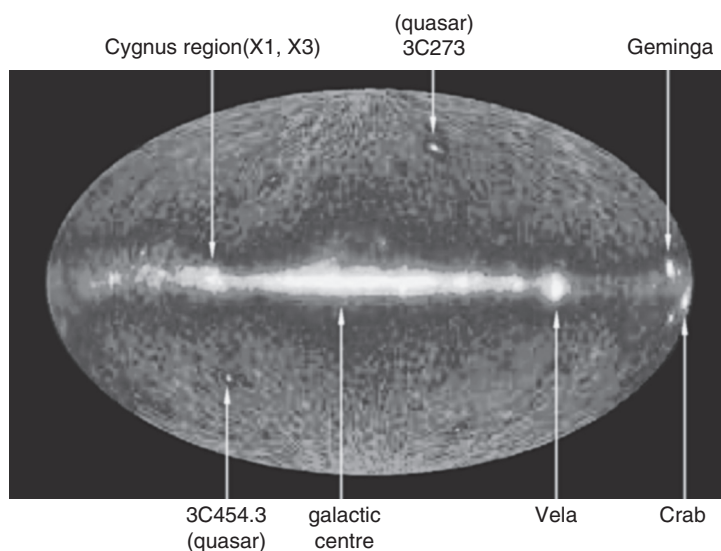


Fig. 16.33. All-sky survey in the light of gamma rays [60, 61].

$\pm 10^\circ$ galactic latitude. These data were recorded with the SAS-2 satellite [59]. The solid line is the result of a simulation, which assumes that the flux of cosmic γ rays is proportional to the column density of the interstellar gas. In this representation the Vela pulsar appears as the brightest γ -ray source in the energy range greater than 100 MeV.

In an all-sky survey with γ -ray detectors on board the Compton Gamma Ray Observatory (CGRO) a large number of γ -ray sources, including extragalactic ones, could be discovered (Fig. 16.33).

16.12 Measurement of extensive air showers with the Fly's Eye detector

High-energy charged particles and photons produce hadronic and electromagnetic cascades in the atmosphere. In a classical technique for registering these *extensive air showers* (EAS) the shower particles are sampled by a large number of scintillation counters or water Cherenkov counters normally installed at sea level [62], like in [63]. The scintillation counters typically cover 1% of the lateral shower distribution and give information on the number of shower particles at a depth far beyond the shower maximum. Clearly, the energy of the primary particle initiating the cascade can only be inferred with a large measurement error. It would be much better to detect the complete longitudinal development of the

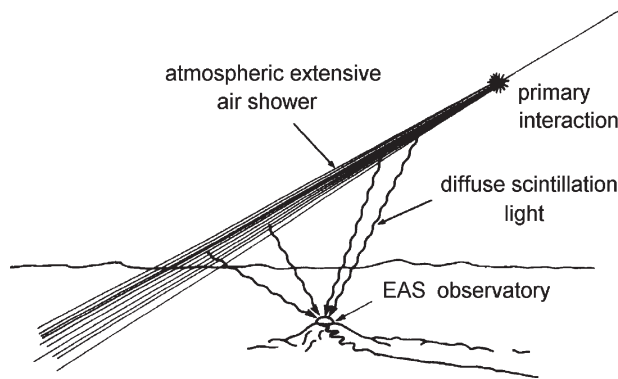
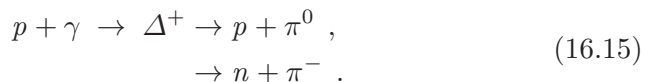


Fig. 16.34. Measurement principle for extensive air showers (EAS) via the scintillation light produced in the atmosphere.

shower in the atmosphere. Such a measurement can be done for energies in excess of 10^{17} eV, if the scintillation light produced by the shower particles in the atmosphere is registered (Fig. 16.34). This can be achieved with the ‘Fly’s Eye’ experiment. The original *Fly’s Eye detector* in Utah consisted of 67 mirrors of 1.6 m diameter each [64–67]. Each mirror had in its focal plane 12 to 14 photomultipliers. The individual mirrors had slightly overlapping fields of view. An extensive air shower passing through the atmosphere in the vicinity of the Fly’s Eye experiment is only seen by some of the photomultipliers. From the fired phototubes, the longitudinal profile of the air shower can be reconstructed. The total recorded light yield is proportional to the shower energy [68].

Such a Fly’s Eye experiment was installed in Utah, USA, for the measurement of high-energy primary cosmic rays (Fig. 16.35). The disadvantage connected with this measurement technique is that the detection of the weak scintillation light can only be done on clear, moonless nights. This detection technique has been further improved with the High Resolution (HiRes) telescope, also in Utah, and the new extended installation, the Telescope Array (TA) which is now under construction at the HiRes site [70]. It is also being used in the larger Auger air-shower array in Argentina [71].

The main scientific aim of these large air-shower arrays is to find the sources of the most energetic cosmic rays and to investigate whether primary protons exceeding a certain threshold energy ($\approx 6 \cdot 10^{19}$ eV) get attenuated by the omnipresent blackbody radiation through the Greisen–Zatsepin–Kuzmin (GZK) cutoff [56] like



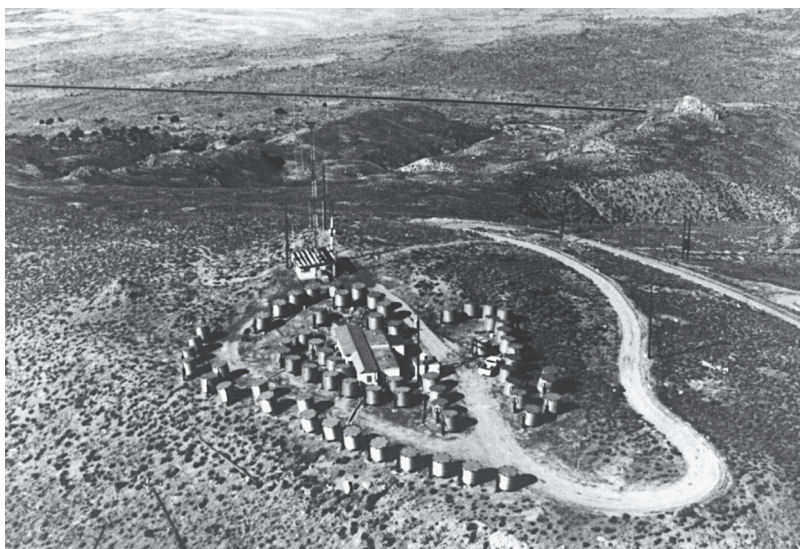


Fig. 16.35. Photograph of the 'Fly's Eye' experiment [64, 69].

Recently, it has been shown that the measurement of geosynchrotron emission in the radio band by the relativistic shower electrons in the Earth's magnetic field presents an attractive alternative for the detection of large air showers [72]. The advantage of this method is its 100% duty time compared to the $\approx 10\%$ duty time of the optical measurement.

The individual mirrors of air-fluorescence detectors can also be separately operated as *Cherenkov telescopes* (e.g. [73, 74]). With such telescopes the Cherenkov radiation of highly relativistic shower particles in the atmosphere is measured. Cherenkov mirror telescopes provide a means to detect γ -ray point sources, which emit in the energy range in excess of 1 TeV. A high angular resolution of these telescopes allows one to suppress the large background of hadron-induced showers, which is isotropically distributed over the sky, and to identify γ -ray-induced cascades from point sources unambiguously. In this particular case one takes advantage of the fact that γ rays travel along straight lines in the galaxy, while charged primary cosmic rays do not carry any directional information on their origin because they become randomised by irregular galactic magnetic fields.

The *imaging air Cherenkov telescopes* (IACT) have provided valuable information on possible sources which are discussed as candidates for the origin of cosmic rays (e.g. the galaxy M87). Up to date such devices (e.g. [74]) can measure primary γ rays down to 20 GeV, thereby widening

the field of view in γ -ray astronomy, because γ rays of this low energy are not absorbed through $\gamma\gamma$ processes in interactions with blackbody or infrared photons.

16.13 Search for proton decay with water Cherenkov counters

In certain theories that attempt to unify the electroweak and strong interactions, the proton is no longer stable. In some models it can decay, violating baryon and lepton conservation number, according to

$$p \rightarrow e^+ + \pi^0 . \quad (16.16)$$

The originally predicted proton lifetime on the order of 10^{30} years requires large-volume detectors to be able to see such rare decays. One possibility for the construction of such a detector is provided by *large-volume water Cherenkov counters* (several thousand tons of water). These Cherenkov detectors contain a sufficiently large number of protons to be able to see several proton decays in a measurement time of several years if the theoretical prediction were correct. The proton-decay products are sufficiently fast to emit Cherenkov light.

Large-volume water Cherenkov detectors require ultra-pure water of high transparency to be able to register the Cherenkov light using a large number of photomultipliers. The phototubes can either be installed in the volume or at the inner surfaces of the detector. Directional information and vertex reconstruction of the decay products is made possible by fast timing methods on the phototubes. Short-range charged particles from nucleon decays produce a characteristic ring of Cherenkov light (Fig. 16.36), where the outer radius r_a is used to determine the distance of the decay vertex from the detector wall and the inner radius r_i approximately reflects the range of the charged particle in water until it falls below the Cherenkov threshold. The measured light yield allows one to determine the energy of the particles.

Two such water Cherenkov detectors were installed in the Kamioka zinc mine in Japan (KamiokaNDE = Kamioka Nucleon Decay Experiment) and the Morton-Thiokol salt mine in Ohio, USA (Irvine–Michigan–Brookhaven (IMB) experiment) [75–77].

In spite of running these detectors over several years, no proton decay was detected. From this result, new limits on the lifetime of the proton were determined to be $\tau \geq 10^{33}$ years.

The large-volume water Cherenkov counters have been spectacularly successful, however, in registering neutrinos emitted by the supernova

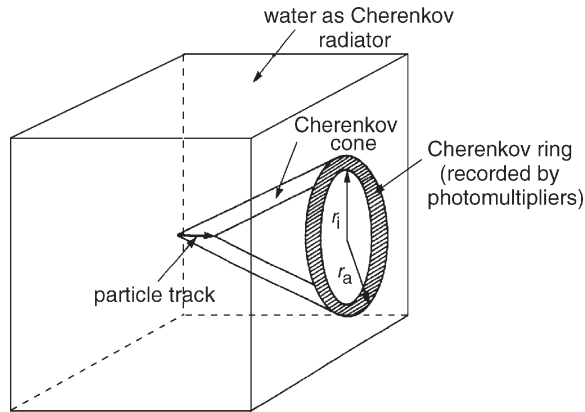


Fig. 16.36. Principle of Cherenkov-ring production in an experiment searching for proton decay.

1987A. The KamiokaNDE, SuperKamiokande and SNO (Sudbury Neutrino Observatory) experiments were even able to detect solar neutrinos because of their low detection threshold for electron energies [76, 78].

The precise measurement of solar and atmospheric neutrinos with these detectors led to the discovery of neutrino oscillations, a major step for discovering physics beyond the Standard Model of elementary particles. The big *sea-water* and *ice Cherenkov counters* have also opened up a new window for astronomy. Meaningful neutrino telescopes for the detection of energetic galactic and extragalactic neutrinos, however, have to be much larger. Such devices are presently being built in the antarctic (*IceCube*) and prepared in the Mediterranean. For precision results on high-energy neutrino astronomy detectors even larger than IceCube will be required. To instrument larger volumes with photomultipliers on strings is prohibitive for cost reasons. However, a new technique of measuring the sound waves associated with energetic interactions in the antarctic ice using *glaciophones* looks promising. The thermoacoustically generated sound waves can be detected by appropriate glaciophones, e.g. by piezo-electric sensors. The main advantage of this technique is that the attenuation of the acoustic signal is very much weaker compared to the optical signal.

16.14 Radio-carbon dating

The dating of archaeological objects of biological origin can be performed with the *radio-carbon dating* method [79, 80]. The Earth's atmosphere

contains in its carbon dioxide the continuously produced radioisotope ^{14}C . This radioisotope is produced by secondary neutrons in cosmic radiation via the reaction



^{14}C is a β^- emitter with a half-life of 5730 years. It decays back into nitrogen according to



In this way a concentration ratio of

$$r = \frac{N({}^{14}_6\text{C})}{N({}^{12}_6\text{C})} = 1.2 \cdot 10^{-12} \quad (16.19)$$

is formed. All plants and, as a consequence of eating vegetable matter, also animals and humans have ^{14}C . Therefore, the isotopic ratio produced in the atmosphere is also formed in the entire biosphere. With the death of a living organism the radio-carbon incorporation comes to an end. The radioactive decay of ^{14}C now reduces the $^{14}\text{C}/^{12}\text{C}$ ratio. By comparing the ^{14}C activity of an archaeological object and a biological object with the equilibrium value of the present time, the age of the object can be determined.

An experimental problem arises because of the low beta activity of archaeological objects. The maximum energy of the electrons emitted in the ^{14}C decay is only 155 keV. Therefore, a very sensitive detector is required for their detection. If the radioisotope ^{14}C is part of a gas ($^{14}\text{CO}_2$), a methane-flow counter can be used (a so-called low-level counter). This detector has to be shielded passively by lead and actively by anti-coincidence counters against background radiation. The methane-flow counter is constructed in such a way that the sample to be investigated – which does not necessarily have to be in the gaseous state – is introduced into the detector volume. This is to prevent energy losses of electrons when entering the counter. A steady methane flow through the detector guarantees a stable gas amplification.

Due to systematic and statistical errors, radio-carbon dating is possible for archaeological objects with ages between 1000 and 75 000 years. In recent times, however, it has to be considered that the concentration ratio r is altered by burning ^{14}C -poor fossil fuels and also by nuclear-weapon tests in the atmosphere. As a consequence r is no longer constant in time. Therefore, a time calibration must first be performed. This can be done by measuring the radio-carbon content of a sample of known age [79].

16.15 Accident dosimetry

Occasionally, the problem arises of determining a radiation dose after radiation accidents if no dosimeter information was available. It is possible to estimate the body dose received after the accident has happened by the *hair-activation method* [81]. Hair contains sulphur with a concentration of 48 mg S per gram hair. By neutron irradiation (e.g. after reactor accidents) the sulphur can be converted to phosphorus according to



In this reaction the radioisotope ${}^{32}\text{P}$ is produced, which has a half-life of 14.3 days. In addition to this particular reaction, the radioactive isotope ${}^{31}\text{Si}$ is formed in the following manner:



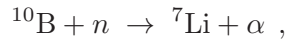
The ${}^{31}\text{Si}$ isotope renders the determination of the phosphorus activity difficult. The half-life of ${}^{31}\text{Si}$, however, is only 2.6 hours. Therefore one waits for a certain amount of time until this activity has decayed before attempting to measure the ${}^{32}\text{P}$ activity. In case of surface contaminations, careful cleaning of the hair has to precede the activity measurement.

${}^{32}\text{P}$ is a pure β -ray emitter. The maximum energy of the electrons in this decay is 1.71 MeV. Because of the normally low expected event rates, a detector with high efficiency and low background is required. An actively and passively shielded end-window counter is a suitable candidate for this kind of measurement. Knowing the activation cross section for the Reaction (16.20), the measured ${}^{32}\text{P}$ activity can be used to infer the radiation dose received.

16.16 Problems

- 16.1** Particle-detector systems are frequently calibrated with laser beams; e.g., laser beams produce straight tracks in a time-projection chamber to monitor the field uniformity or the drift velocity. Also for air Cherenkov telescopes or air scintillation telescopes laser calibration is employed. What is the force experienced by a detector when it is hit by a 10 mW laser beam of which a fraction $\epsilon = 50\%$ is reflected?

- 16.2** Carbon-14 dating works well if the age of the samples to be age-determined is on the order of magnitude of its half-life. For geological lifetimes other techniques must be employed. The primordial isotope ^{238}U has a half-life of $4.51 \cdot 10^9$ years. It decays eventually via thorium, actinium, radium, radon and polonium into the stable lead isotope ^{206}Pb . In a rock sample an isotopic ratio of $r = N(^{206}\text{Pb})/N(^{238}\text{U}) = 6\%$ is found. What is the age of the rock if all the ^{206}Pb has been produced by ^{238}U and if all other half-lives in the decay chain can be neglected?
- 16.3** A geostationary air-watch satellite to measure the scintillation light produced by extensive air showers in the atmosphere is naturally exposed to sunlight for almost all of its orbit. What kind of temperature will the satellite get if its emissivity and absorption – assumed to be the same – are independent of the frequency?
- 16.4** Neutron detection is frequently done with BF_3 counters using the reaction



where the Q value of the reaction for reaching the ground state of ^7Li is 2.8 MeV. What fraction of this energy goes to the α particle?

- 16.5** The luminosity at e^+e^- colliders is normally determined by small-angle elastic scattering (called Bhabha scattering in this case). For that purpose track-sensitive electromagnetic calorimeters are installed close to the beam line in backward and forward direction. In these forward calorimeters with an acceptance starting at a polar angle of θ_0 (typically 30 mrad) high rates of scattered e^+e^- events (Bhabha events) are measured. The neutral-current Z exchange does not contribute at small scattering angles. In a measurement of the cross section for $\sigma(e^+e^- \rightarrow Z \rightarrow \text{hadrons})$ the accuracy is determined by the precision of the luminosity measurement. If the statistical error of the luminosity determination dominates, and if the accuracy for the Z cross section has to be improved by a factor of 2, by how much would the luminosity calorimeters have to be moved closer to the beam (θ_{new})?
- 16.6** Air Cherenkov telescopes measure the Cherenkov light emitted from electrons and positrons which are produced in the process of the development of the induced electromagnetic cascade. At 100 GeV primary photon energy the shower does not reach sea level. Therefore, conventional air-shower techniques using

ground-level particle sampling have no chance to measure primary photons of this energy. Estimate the number of photons per m^2 produced by a 100 GeV γ ray from some galactic source at sea level.

For details of electromagnetic showers see Sect. 8.1.

References

- [1] K. Kleinknecht, *Detektoren für Teilchenstrahlung*, Teubner, Stuttgart (1984, 1987, 1992); *Detectors for Particle Radiation*, Cambridge University Press, Cambridge (1986)
- [2] P.B. Cushman, Electromagnetic and Hadronic Calorimeters, in F. Sauli (ed.), *Instrumentation in High Energy Physics*, World Scientific, Singapore (1992)
- [3] N.A. Dyson, *Nuclear Physics with Application in Medicine and Biology*, John Wiley & Sons Inc. (Wiley Interscience), New York (1981); *Radiation Physics with Applications in Medicine and Biology*, Ellis Horwood, New York (1993)
- [4] F. Sauli, *Applications of Gaseous Detectors in Astrophysics, Medicine and Biology*, CERN-PPE-92-047; *Nucl. Instr. Meth.* **323** (1992) 1–11
- [5] K. Siegbahn (ed.), *Alpha, Beta and Gamma-Ray Spectroscopy*, Vol. 1 and Vol. 2, Elsevier–North Holland, Amsterdam (1968)
- [6] F. Sauli (ed.), *Instrumentation in High Energy Physics*, World Scientific, Singapore (1992)
- [7] T. Ferbel (ed.), *Experimental Techniques in High Energy Nuclear and Particle Physics*, World Scientific, Singapore (1991)
- [8] S. Hayakawa, *Cosmic Ray Physics*, John Wiley & Sons Inc. (Wiley Interscience), New York (1969)
- [9] K. Kleinknecht & T.D. Lee (eds.), *Particles and Detectors; Festschrift for Jack Steinberger*, Springer Tracts in Modern Physics Vol. 108, Springer, Berlin/Heidelberg (1986)
- [10] D.J. Miller, Particle Physics and its Detectors, *Nucl. Instr. Meth.* **310** (1991) 35–46
- [11] G. Hall, Modern Charged Particle Detectors, *Contemp. Phys.* **33** (1992) 1–14
- [12] W.C. Röntgen, *Eine neue Art von Strahlen*, Sitzungsberichte der Würzburger Physikalisch-medicinischen Gesellschaft, Würzburg (December 1895)
- [13] Otto Glasser, *Wilhelm Conrad Röntgen and the Early History of the Röntgen Rays*, National Library of Medicine, London (1933)
- [14] RadiologyInfo, Radiological Society of North America, Inc. (RSNA) (2006); www.radiologyinfo.org/en/photocat/photos_more_pc.cfm?pg=bonerad
- [15] E. Hell, W. Knüpfner & D. Mattern, The Evolution of Scintillating Medical Detectors, *Nucl. Instr. Meth.* **A454** (2000) 40–8
- [16] H.O. Anger, Scintillation Camera, *Rev. Sci. Instr.* **2a** (1958) 27–33

- [17] H.O. Anger, Scintillation Camera with Multichannel Collimators, *J. Nucl. Med.* **5** (1964) 515–31
- [18] R.W. Todd, J.M. Nightingale & D.B. Everett, A Proposed γ -Camera, *Nature* **251** (1974) 132–4; J.B. Martin *et al.*, A Ring Compton Scatter Camera for Imaging Medium Energy Gamma Rays, *IEEE Trans. Nucl. Sci.* **49(3)**, Part 1 (2002) 817–21; T. Conka-Nurdan *et al.*, Silicon Drift Detector Readout Electronics for a Compton Camera, *Nucl. Instr. Meth.* **A523(3)** (2004) 435–40
- [19] G. Montgomery, *The Mind in Motion*, Discover, Charlottesville, VA (1989) 58–61
- [20] V.J. Stenger, *Physics and Psychics*, Prometheus, Buffalo, New York (1990)
- [21] Solomon H. Snyder, *Frontiers of Science*, National Geographic Society, Library of Congress (1982)
- [22] www.triumf.ca/welcome/petscan.html
- [23] W. Thomlinson & D. Chapman, private communication (2005)
- [24] St. Fiedler, *Synchrotron Radiation Angiography: Dead Ends and Perspectives*; www.lightsource.ca/bioimaging/Saskatoon_2004_sf.pdf
- [25] H. Elleaume, S. Fiedler, B. Bertrand, *et al.*, First Human Transvenous Coronary Angiography Studies at the ESRF, *Phys. Med. Biol.* **45** (2000) L39–L43
- [26] J.R. Schneider, HasyLab; wissenschaftlicher Jahresbericht DESY (2000) 116–28
- [27] T. Dill *et al.*; Intravenous Coronary Angiography with the System NIKOS IV, www-hasyLab.desy.de/science/annual_reports/1998/part1/contrib/26/2601
- [28] www.physik.uni-siegen.de/walenta/angio/index.html
- [29] G. Kraft, *Radiobiology of Heavy Charged Particles*, GSI preprint 96-60 (November 1996)
- [30] G. Kraft, *Tumour Therapy with Ion Beams*, invited paper at the SAMBA Symposium at the University of Siegen 1999, *Nucl. Instr. Meth.* **A454** (2000) 1–10
- [31] G. Kraft, The Impact of Nuclear Science on Medicine, *Nucl. Phys.* **A654** (1999) 1058C–67C
- [32] G. Kraft, Radiotherapy with Heavy Charged Particles, www.gsi.de
- [33] Medical Radiation Group, National Accelerator Center South Africa, www.nac.ac.za/public; Brochure for Specialised Radiotherapy, www.nac.ac.za/public/default.htm; U. Amaldi & G. Kraft, Radiotherapy with Beams of Carbon, *Rep. Progr. Phys.* **68** (2005) 1861–82
- [34] S.B. Curtis & M.R. Raju, A Calculation of the Physical Characteristics of Negative Pion Beams Energy Loss, Distribution and Bragg Curves, *Radiat. Res.* **34** (1968) 239–47
- [35] C.L. Briant & R.P. Messmer, *Auger Electron Spectroscopy (Treatise on Materials Science and Technology)*, Academic Press, Cambridge (1988); M. Prutton & M.M. El Gomati, *Scanning Auger Electron Microscopy*, John Wiley & Sons Inc., New York (2006)

- [36] S.E. Hunt, *Nuclear Physics for Engineers and Scientists*, John Wiley & Sons Inc. (Wiley Interscience), New York (1987)
- [37] C. Grupen, *Grundkurs Strahlenschutz*, Springer, Berlin (2003)
- [38] James E. Martin, *Physics for Radiation Protection*, John Wiley & Sons Inc., New York (2000)
- [39] Bicron, Detector Application, Information Note: Geological Exploration, Newbury, Ohio, USA (1997)
- [40] S. Sailer, Daimler Benz AG, Central Materials Technology, Stuttgart, Proceedings of the International Atomic Energy Agency (1982)
- [41] A. Gerve, The Most Important Wear Methods of Isotope Technology, *Kerntechnik* **14** (1972) 204–12
- [42] U. Braun, *Messung der Radioaktivitätskonzentration in biologischen Objekten nach dem Reaktorunfall in Tschernobyl und ein Versuch einer Interpretation ihrer Folgen*, Diploma Thesis, University of Siegen (1988)
- [43] C. Grupen *et al.*, *Nuklid-Analyse von Beta-Strahlern mit Halbleiterspektrometern im Fallout*, Symp. *Strahlenmessung und Dosimetrie*, Regensburg (1966) 670–81
- [44] L. Alvarez *et al.*, Search for Hidden Chambers in the Pyramids, *Science* **167** (1970) 832–9
- [45] F. El Bedewi *et al.*, Energy Spectrum and Angular Distribution of Cosmic Ray Muons in the Range 50–70 GeV, *J. Phys.* **A5** (1972) 292–301
- [46] H. Tanaka *et al.*, Development of a Two-fold Segmented Detection System for Near Horizontally Cosmic-Ray Muons to Probe the Internal Structure of a Volcano, *Nucl. Instr. Meth.* **A507** (2003) 657–69
- [47] L. Smolik, private communication (2006); L. Smolik, *True Random Number Generation Using Quantum Mechanical Effects*, Proc. of Security and Protection of Information 2003, pp. 155–60, Brno (Brünn), Czech Republic (2003)
- [48] C. Grupen, I. Maurer, S. Schmidt & L. Smolik, *Generating Cryptographic Keys by Radioactive Decays*, 3rd International Symposium on Nuclear and Related Techniques, 22–26 October 2001, NURT, Cuba, ISBN 959-7136-12-0 (2001)
- [49] L. Smolik, F. Janke & C. Grupen, Zufallsdaten aus dem radioaktiven Zerfall, *Strahlenschutzpraxis* Heft 2 (Mai 2003) 55–7
- [50] G. Danby, J.M. Gaillard, K. Goulianos, L.M. Lederman, N. Mistry, M. Schwartz & J. Steinberger (Columbia U. and Brookhaven) 1962, Observation of High Energy Neutrino Reactions and the Existence of Two Kinds of Neutrinos, *Phys. Rev. Lett.* **9** (1962) 36–44
- [51] *Oscillating Neutrinos*, CERN-Courier **20(5)** (1980) 189–90
- [52] O.C. Allkofer, W.D. Dau & C. Grupen, *Spark Chambers*, Thiemig, München (1969)
- [53] H. Faissner, *The Spark Chamber Neutrino Experiment at CERN*, CERN-Report **63-37** (1963) 43–76
- [54] R. Hillier, *Gamma Ray Astronomy*, Clarendon Press, Oxford (1984)
- [55] P.V. Ramana Murthy & A.W. Wolfendale, *Gamma Ray Astronomy*, Cambridge University Press, Cambridge (1986)

- [56] C. Grupen, *Astroparticle Physics*, Springer, New York (2005)
- [57] G.F. Bignami *et al.*, The COS-B Experiment for Gamma-Ray Astronomy, *Space Sci. Instr.* **1** (1975) 245–52; ESRO: The Context and Status of Gamma Ray Astronomy (1974) 307–22
- [58] Photo MBB-GmbH, *COS-B, Satellit zur Erforschung der kosmischen Gammastrahlung*, Unternehmensbereich Raumfahrt, München (1975)
- [59] C.E. Fichtel *et al.*, SAS-2 Observations of Diffuse Gamma Radiation in the Galactic Latitude Interval $10^\circ < |b| \leq 90^\circ$, *Astrophys. J. Lett. Ed.* **217(1)** (1977) L9–L13; *Proc. 12th ESLAB Symp.*, Frascati (1977) 95–9
- [60] CGRO-project, Scientist Dr. Neil Gehrels, Goddard Space Flight Center, <http://coss.gsfc.nasa.gov/docs/cgro/index.html> (1999)
- [61] <http://coss.gsfc.nasa.gov/docs/cgro/coss/coss.html>
- [62] P. Baillon, *Detection of Atmospheric Cascades at Ground Level*, CERN-PPE-91-012 (1991)
- [63] M. Teshima *et al.*, Expanded Array for Giant Air Shower Observation at Akeno, *Nucl. Instr. Meth.* **A247** (1986) 399–411; M. Takeda *et al.*, Extension of the Cosmic-Ray Energy Spectrum beyond the Predicted Greisen-Zatsepin-Kuz'min Cutoff, *Phys. Rev. Lett.* **81** (1998) 1163–6; K. Shinozaki & M. Teshima, AGASA Results, *Nucl. Phys. B Proc. Suppl.* **136** (2004) 18–27
- [64] R.M. Baltrusaitis *et al.*, The Utah Fly's Eye Detector, *Nucl. Instr. Meth.* **A240** (1985) 410–28
- [65] J. Linsley, The Highest Energy Cosmic Rays, *Scientific American* **239(1)** (1978) 48–65
- [66] J. Boone *et al.*, *Observations of the Crab Pulsar near 10^{15} – 10^{16} eV*, 18th Int. Cosmic Ray Conf. Bangalore, India, Vol. 9 (1983) 57–60; University of Utah, UU-HEP 84/3 (1984)
- [67] G.L. Cassiday *et al.*, Cosmic Rays and Particle Physics, in T.K. Gaisser (ed.), *Am. Inst. Phys.* **49** (1978) 417–41
- [68] C. Grupen, Kosmische Strahlung, *Physik in unserer Zeit* **16** (1985) 69–77
- [69] G.L. Cassiday, private communication (1985)
- [70] High Resolution Fly's Eye: <http://hires.physics.utah.edu/>; and www.telescopearray.org/
- [71] Auger collaboration, www.auger.org/
- [72] H. Falcke *et al.* – LOPES Collaboration, Detection and Imaging of Atmospheric Radio Flashes from Cosmic Ray Air Showers, *Nature* **435** (2005) 313–6
- [73] HESS collaboration, www.mpi-hd.mpg.de/hfm/HESS/
- [74] MAGIC collaboration, www.magic.mppmu.mhg.de/collaboration/
- [75] K.S. Hirata *et al.*, Observation of a Neutrino Burst from the Supernova SN 1987 A, *Phys. Rev. Lett.* **58** (1987) 1490–3
- [76] K.S. Hirata *et al.*, *Observation of 8B Solar Neutrinos in the Kamiokande II Detector*, Inst. f. Cosmic Ray Research, ICR-Report 188-89-5 (1989)
- [77] R. Bionta *et al.*, Observation on a Neutrino Burst in Coincidence with Supernova SN 1987 A in the Large Magellanic Cloud, *Phys. Rev. Lett.* **58(14)** (1987) 1494–6

- [78] www.sno.phy.queensu.ca/
- [79] W. Stolz, *Radioaktivität*, Hanser, München/Wien (1990)
- [80] M.A. Geyh & H. Schleicher, *Absolute Age Determination: Physical and Chemical Dating Methods and Their Application*, Springer, Berlin (1990)
- [81] E. Sauter, *Grundlagen des Strahlenschutzes*, Siemens AG, Berlin/München (1971); *Grundlagen des Strahlenschutzes*, Thiemig, München (1982)